PAPER

Segregation effects on the properties of (AuAg)$_{147}$†

A. L. Gould,*[a] C. J. Heard,[b] A. J. Logsdail*[c] and C. R. A. Catlow[ac]

AuAg nanoclusters are promising supported co-catalysts for photocatalytic hydrogen reduction. However, beyond the quantum regime ($N > 100$) little is known about how the electronic properties of these nanoparticles are affected by chemical ordering. We investigate the effects of chemical ordering on the properties of 147-atom cuboctahedral AuAg nanoclusters, using empirical potentials coupled with an atomic-swap basin-hopping search to optimise the elemental distribution, with the lowest energy arrangements then reminimised using Density Functional Theory (DFT). Force-field calculations show Au atoms preferentially occupy sub-surface positions in the bimetallic structures, which results in the formation of a pseudo-onion structure for Ag-rich compositions. At the DFT-level, however, an Ag core surrounded by an Au shell (Ag@Au) is energetically favoured, as electron density can be drawn more readily when Au atoms are positioned on the nanocluster surface, thus resulting in a partial negative charge. Core@shell configurations are analogous to structures that can be chemically synthesised, and further detailed electronic analysis is discussed in the context of nanocluster applications to co-catalysed photocatalysis.

[a] *Rutherford Appleton Laboratory, Harwell Oxford Didcot, Oxon, OX11 0FA, UK.*
E-mail: a.gould@ucl.ac.uk
[b] *School of Chemistry, University of Birmingham, Edgbaston, Birmingham,*
B15 2TT, UK
[c] *Kathleen Lonsdale Materials Chemistry, 20 Gordon Street, London, WC1H 0AJ,*
UK. E-mail: a.logsdail@ucl.ac.uk

† Electronic supplementary information (ESI) available: Figure of geometrically decomposed atomic arrangement for Au$_{13}$Ag$_{134}$ and Au$_{55}$Ag$_{92}$ alloys; table of the differences in E_b and E_{exc} for all investigated systems, along with E_F; plot of E_b^{Gupta} and E_b^{DFT} against σ; plots of the DOS for alloy and core@shell structures with varying Ag : Au ratios. See DOI: 10.1039/c4cp00753k

1. Introduction

Supported metal nanoparticles (nanoclusters) can enhance heterogeneous catalysis in comparison to isolated supports or nanoclusters,[1,2] with the structure of the nanocluster greatly influencing catalytic performance.[3] Recently, nanoclusters have been used successfully as co-catalysts for photocatalytic reactions on semiconducting substrates, using both visible and ultraviolet light sources.[4] Two distinct physical processes are thought to occur in the synthesis routes: for visible-light (2–3 eV), surface plasmon resonances result in the direct injection of electrons from the nanocluster into the semiconductor conduction band,[5] whereas for UV radiation (3–10^3 eV), direct excitation of electrons from the valence band of the semiconductor to the conduction band occurs, with nanoclusters then acting as an electron trap for the excited states, thus extending the photocatalytic lifetime.[6]

Bimetallic nanoclusters ("nanoalloys") have garnered much recent interest, as the combination of two metallic species can result in favourable synergistic effects, and lower production costs.[7] The introduction of a second metal, however, significantly complicates the nanocluster structure, as there is a range of possible chemical arrangements for the two elements. The three most common chemical orderings are mixed nanoalloys, segregated subclusters and core@shell segregated nanoalloys.[8,9] The quantity of different chemical arrangements, or "homotops",[10,11] for a bimetallic nanocluster A$_{N_A}$B$_{N_B}$ is defined as:

$$N_H = \frac{N!}{N_A! N_B!} \equiv \frac{N!}{N_A!(N - N_A!)} \tag{1}$$

where N is the number of atoms in the cluster, N_H is the number of possible homotops, N_A is the number of atoms of type A, and N_B is the number of type B.[12] As N increases, N_H becomes extremely large in 1 : 1 alloy systems, although symmetric equivalence in the chemical arrangements can be used to simplify analysis.[13]

In general, the geometric preferences of nanoclusters depend strongly on factors such as the atomic size, electronegativity and electronic charge for the constituent species.[14,15] Compact, non-crystalline structures often form for small nuclearities (N), minimising surface area at the expense of increased internal strain due to the non-optimal internal interatomic distances.[16] Strain energy is generally proportional to cluster volume, so the non-crystalline structures become energetically unfavourable at large N, instead forming more

This journal is © the Owner Societies 2014

Phys. Chem. Chem. Phys., 2014, **16**, 21049–21061 | **21049**

bulk-like arrangements where the strain energy is reduced. For bimetallic systems, atomic size mismatch between species can play an important role in the reduction of the structure-induced strain energy.[17] If atomic size mismatch is large, the overall strain energy can be reduced for non-crystalline structures by placing the smaller atoms inside the nanoalloy, as observed for Ag–Ni, Ag–Cu and Au–Cu.[14]

Previous studies have highlighted three prominent high symmetry structures for nanoclusters: the icosahedron (Ih), the Ino-decahedron (I-Dh) and the cuboctahedron (CO); each of which form closed shell geometries at equivalent N.[18,19] Small clusters favour the Ih, where minimisation of the surface energy takes precedence over strain contributions.[20] I-Dh has less internal strain than Ih, and is therefore favoured at larger N. CO is a face-centred cubic (FCC) fragment and therefore has the lowest internal strain of these geometries (arising in nanoclusters due to surface contractions). However, it has the largest surface/volume ratio, and thus is favoured at sizes tending to the bulk ($N \to \infty$).[16]

Geometrically complete atomic shells are achieved at the same nuclearities for Ih, I-Dh and CO, and are referred to as "magic numbers" due to the particularly high geometric stabilities encountered.[21] Equivalent electronic stability is achieved for "magic numbers" of electrons when the total number of valence electrons results in a complete valence shell ($1s^2$, $2s^2$, $2p^6$,...). These magic clusters are of experimental interest as their high stability results in monodisperse systems, and the clusters can therefore be identified as particularly strong peaks in mass spectra, indicative of their greater stability with respect to dissociation when compared to neighbouring sizes.[22]

AuAg nanoalloys are of recent interest as they have been shown to improve catalytic activity for CO and H_2 oxidation,[23] and reduce production costs.[24] However, they are a complex system to study as the mismatch in atomic size is small, and coupled with their significantly differing electronegativities (2.54 for Au and 1.93 for Ag[25]), the formation of alloys during chemical synthesis is common. An appreciable degree of charge transfer may occur between the elements, due to the differing electronegativities, which can affect atomic radii and mitigates against the stability of chemical arrangements such as core@shell.[17] Experimental synthesis of core@shell structural arrangements, however, has been demonstrated as feasible due to kinetic trapping.[26–29]

To discuss the thermodynamic stability of AuAg nanoclusters, we need to consider the bulk properties of Au and Ag. The homogeneous bond lengths are very similar: 2.889 and 2.884 Å for Ag and Au, respectively,[30] meaning that there is minimal size mismatch between the two atomic species, and thus a minimal strain-induced driving force for segregation. However, the surface energy of Ag is less than that of Au (78 and 97 meV Å^{-2} respectively[31]), which would favour surface segregation of Ag atoms. The cohesive energy of Ag is also lower than that of Au: 2.95 eV atom^{-1} compared to 3.81 eV atom^{-1}, respectively,[32] which implies preferential segregation of Au atoms towards a nanocluster core, where they will have a higher coordination.[33]

Previous computational work has thoroughly investigated the structural preferences for small Au[34–38] and Ag[39–43] nanoclusters,

however AuAg is less well studied. Higher-level DFT calculations for small AuAg nanoalloys ($N \leq 10$ atoms[37]) have shown a preference for topologies that maximise the number of Au–Ag interactions, allowing for improved charge transfer between the two metallic species.[44,45] In these small clusters the adopted chemical order can induce further charge transfer than initially expected, as found by Chen et al. for $(AuAg)_{13}$.[33] Bonačić-Koutecký observed planar structures were favoured for Au_4Ag_4 and Ag_8, due to dominant s-orbital bonding, whilst the favoured arrangement of Au_8 is less clear; Bonačić-Koutecký found 3D structures, attributed to the participation of d electrons,[46] whereas Heiles et al. determined Au_8 to be planar.[45]

Larger nanoalloys ($10 \leq x \leq 100$ atoms) favour structures that have an Ag-enriched surface and an Au-enriched core, as calculated using a combined empirical potentials and DFT approach,[47–50] although a recent basin-hopping study by Cerbelaud et al., using an empirical potential that incorporates charge transfer effects, finds that Au atoms on the nanoalloy surface are energetically favourable and in better agreement with equivalent DFT calculations up to $N = 201$.[51] Most recently, the kinetic ordering in 55-atom icosahedral AuAg clusters were investigated by Calvo et al.,[52] using discrete-path sampling with empirical potentials. Inversion of core@shell structures from Au@Ag to Ag@Au required compositional rearrangement (rather than diverse atomistic mechanisms) in two stages; firstly the migration of many atoms, breaking icosahedral symmetry, followed by the introduction of vacancies. Spontaneous reordering under ambient conditions was determined to be very unlikely, due to an overall forward (backward) energy barrier of 2.74 (0.62) eV.

For $N < 100$, the properties of the clusters are often governed by quantum effects where "every atom counts"; however, the electronic properties of larger clusters ($N > 100$) should become more consistent with variation in N, and so observations made for large N may be extrapolated for comparison with even larger experimental clusters. Therefore, in this work we examine the energetically favourable chemical ordering for different AuAg nanoclusters beyond the quantum regime, using a representative 147-atom CO. The chemical orderings were optimised (with respect to the energy of the nanocluster) for various stoichiometries using semi-empirical potentials with atomic-swap searches, and the lowest energy structures have then been reminimised at the DFT-level, and reanalysed. By determining the most stable and/or the most catalytically suitable arrangements, particular morphologies may be proposed for experimental synthesis in the highlighted photocatalytic applications.

2. Theoretical methods

A 147-atom CO nanocluster [Fig. 1(a)] was created using mathematical constructs. Starting with pure Ag_{147}, the Au content was systematically increased until the final composition reached Au_{147}. The optimisation of chemical ordering was investigated for $Au_{147-n}Ag_n$, where $n = 1, 13, 55, 73, 92, 134$
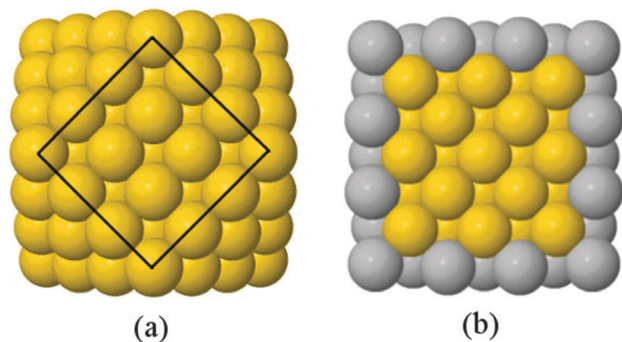
21050 | *Phys. Chem. Chem. Phys.*, 2014, **16**, 21049–21061

This journal is © the Owner Societies 2014

Fig. 1 Examples of the cuboctahedral structure: (a) Au$_{147}$; and (b) a cross section of Au$_{55}$@Ag$_{92}$ core@shell structure. Yellow and grey spheres represent Au and Ag, respectively. For clarity, the (100) surface in (a) has been highlighted with a black line.

and 146. Our choices of n are such that the ratios of Ag : Au allow geometric "magic number" [n = 13, 55, 92, 134] core@-shell arrangements to be formed [Fig. 1(b)]. We also investigated 1 : 1 alloys [n = 73] and atomically doped systems [n = 1, 146].

2.1 The Gupta potential

To improve computational feasibility we have used semi-empirical potentials in our initial searches for optimal chemical ordering; the potentials are fitted to an assumed functional form that reproduces bulk properties. The Gupta potential, commonly used to model interatomic interactions for metallic systems,[53] has previously been successful applied to problems of a similar nature to ours.[54–56] It is derived from the second moment approximation to tight-binding theory, where atoms are modelled as rigid ions, and electrons are allowed to 'hop' between.[57] The truncated form consists of an attractive many body (V_i^{m}) and a repulsive pair (V_i^{r}) term, obtained by summing over all N atoms, to give a total energy:

$$V_{\mathrm{clus}} = \sum_{i=0}^{N} \left(V_i^{\mathrm{r}} - V_i^{\mathrm{m}} \right). \tag{2}$$

V_i^{r} and V_i^{m} are defined as:

$$V_i^{\mathrm{r}}\left(r_{ij}\right) = \sum_{j \neq i}^{N} A \mathrm{e}^{-p\left(\frac{r_{ij}}{r_0}-1\right)} \tag{3}$$

and:

$$V_i^{\mathrm{m}}\left(r_{ij}\right) = \left[\sum_{j \neq i}^{N} \xi^2 \mathrm{e}^{-2q\left(\frac{r_{ij}}{r_0}-1\right)} \right]^{\frac{1}{2}} \tag{4}$$

where r_{ij} is the interatomic distance between atoms i and j, and r_0 is the equilibrium bond length. All other potential parameters (A, p, ξ and q) are fitted to reproduce experimental values for the cohesive energy, lattice parameters and independent elastic constants for the bulk crystal at 0 K. The parameters used in this study are taken from the work of Cleri and Rosato,[30] and are presented in Table 1.

Table 1 Gupta potential parameters as given by Cleri & Rosato.[30] Au–Ag parameters are the arithmetic mean of the pure parameters

Parameter	A/eV	r_0/Å	ξ/eV	p	q
Au–Au	0.2061	2.8843	4.036	10.229	1.790
Au–Ag	0.15445	2.8864	3.5875	10.5785	1.484
Ag–Ag	0.1028	2.8885	3.139	10.928	1.178

2.2 Basin-hopping algorithm

Searches for the optimal chemical ordering of the nanocluster were performed using the basin-hopping (BH) algorithm as implemented in the software package GMIN.[58] More explicitly, the atomic swap functionality was used exclusively, rather than full basin-hopping, where two atoms are randomly selected, and their coordinates are interchanged. By using just the atomic-swap functionality, we ensure that the starting CO structure is maintained throughout.

For each chemical composition we have investigated, a 500 000-iteration search was performed, with between 0 and 147 atomic random swaps at each step, and the new chemical arrangement then energetically reminimised. The geometry and energies of the lowest energy structures were stored throughout. In all cases, there was no variation in the lowest energy arrangements near to the final iterations of the search, and thus the number of iterations, and atomic swaps, were deemed to be sufficiently converged.

2.3 Density functional theory (DFT)

The lowest energy structures were reminimised using DFT, as implemented by the projector-augmented wave method (PAW).[59] Grid-based PAW (GPAW) uses a real-space grid, transforming the wavefunctions at the core to a smooth pseudo-wavefunction.[60] The transformation [T] is specified by a set of all-electron partial waves, a set of pseudo partial waves, and a set of projector functions. The projector functions are what join (or augment) together the two solutions at a certain radius.[61] Both Au and Ag have 11 valence electrons in our setup, and we used converged grid spacings of 0.18 for the numerical representation of the wavefunctions, and vacuum regions of 6 Å around the nanocluster, thus ensuring that no spurious energies or cut-off artefacts were encountered. For the geometry optimisations, convergence was achieved when the forces on all atoms were reduced below 0.01 eV Å^{-1}.

We have used the generalized gradient approximation (GGA) of Perdew, Burke and Ernzerhof (PBE) exchange–correlation functional,[62] with the residual minimisation method, direct inversion in iterative subspace (RMM-DIIS) for spin-polarized calculations throughout. The calculations included 1617 explicit valence electrons and the initial magnetic moment (μ) of the nanocluster was set to 1, to account for a single unpaired electron. During the calculations, however, μ was allowed to relax dynamically, and tended towards μ = 0 in all cases; this observation was supported by the spin contamination, $\langle S^2 \rangle$, which also tended to 0. This resultant singlet state is an artefact of the DFT method, but the overall effect on geometry, energy and charge density was found to be negligible, due to the

This journal is © the Owner Societies 2014

Phys. Chem. Chem. Phys., 2014, **16**, 21049–21061 | **21051**

delocalised "metallic" nature of the wavefunction at the Fermi Energy (E_F). This was verified by performing fixed-spin DFT calculations, with $\mu = 1$, on the final geometries, for which the difference in energy compared to the spin-paired results was less than 0.4 meV per atom, and consistent in sign for each combinatorial arrangement.

2.4 Energetic analysis

In order to relate the differing stoichiometric compositions of our fixed-size bimetallic clusters, there are several methods of energetic analysis. The simplest observable is the binding energy, E_b:[63]

$$E_b^{\text{Gupta}} = \frac{-E_{\text{tot}}^{\text{Gupta}}}{N},$$ (5)

where $E_{\text{tot}}^{\text{Gupta}}$ represents the total energy of a cluster calculated at the Gupta level. For DFT calculations, E_b^{DFT} is more appropriate, as the free atom ($E_{\text{atom}}^{\text{DFT}}$) has kinetic contributions ($E_{\text{atom}}^{\text{DFT}}$ is calculated as -0.185 and -0.194 eV for Au and Ag, respectively). For a bimetallic cluster with a composition of $A_{N_A}B_{N_B}$:

$$E_b^{\text{DFT}} = \frac{-E_{\text{tot}}^{\text{DFT}} - N E_{\text{atom}}^{\text{DFT}}}{N},$$ (6)

$$= \frac{-E_{\text{tot}}^{\text{DFT}} - N_A E_{\text{atom}}^{A,\text{DFT}} - N_B E_{\text{atom}}^{B,\text{DFT}}}{N}$$ (7)

where $E_{\text{tot}}^{\text{DFT}}$ represents the total energy of a cluster calculated at the DFT level.

The excess energy, E_{exc}, is useful as it highlights the energetic difference between the bulk and nanocluster of interest, and is defined as a function of composition thus:[63]

$$E_{\text{exc}}^{\text{Gupta}} = E_{\text{tot}}^{\text{Gupta}} - N_A(E_{\text{coh,A}}) - N_B(E_{\text{coh,B}})$$ (8)

at the Gupta level, where E_{coh} is the cohesive energy per atom in the bulk of metals A and B, respectively. Similarly, for DFT calculations:

$$E_{\text{exc}}^{\text{DFT}} = E_{\text{tot}}^{\text{DFT}} - N_A(E_{\text{coh,A}}) - N_B(E_{\text{coh,B}})$$ (9)

For Gupta calculations ($E_{\text{exc}}^{\text{Gupta}}$), the parameterised values of E_{coh} are used: 3.779 eV and 2.96 eV for Au and Ag, respectively. For $E_{\text{exc}}^{\text{DFT}}$ we have calculated the values for Au and Ag as 3.25 and 2.75 eV, respectively, using the PBE functional. For comparison, the experimental values for E_{coh} are 3.81 eV for Au and 2.95 eV for Ag.[32]

E_{exc} can be related to the number of surface atoms within a structure, inferring the excess energy of the nanocluster is related to the energy required to create the nanocluster surfaces. The ratio of E_{exc} to the number of surface atoms, approximated as $N^{2/3}$, is written as:[64,65]

$$\Delta_{\text{Gupta}} = \frac{E_{\text{exc}}^{\text{Gupta}}}{N^{2/3}},$$ (10)

or

$$\Delta_{\text{DFT}} = \frac{E_{\text{exc}}^{\text{DFT}}}{N^{2/3}}.$$ (11)

However, when comparing clusters of the same size but of differing compositions, Δ_{Gupta} and Δ_{DFT} can become biased as

metals with larger cohesive energies result in clusters with larger excess energies. Thus, an unbiased alternative is $\Delta_{147}^{\text{Gupta}}$, where E_b^{Gupta} is subtracted instead of the bulk cohesive energies:[66,67]

$$\Delta_{147}^{\text{Gupta}} = E_{\text{tot}}^{\text{Gupta}} - N_A \frac{E_{\text{tot}}^{\text{Gupta}}(A_{147})}{147} - N_B \frac{E_{\text{tot}}^{\text{Gupta}}(B_{147})}{147}$$ (12)

where N_A and N_B are the number of atoms of each metallic elements A and B. $\Delta_{147}^{\text{Gupta}}$ is zero for pure clusters, and negative values of E_{exc} indicate improved stability. The corresponding quantity at the DFT level is:

$$\Delta_{147}^{\text{DFT}} = E_{\text{total}}^{\text{DFT}} - N_A \frac{E_{\text{total}}^{\text{DFT}}(A_{147})}{147} - N_B \frac{E_{\text{total}}^{\text{DFT}}(B_{147})}{147}$$ (13)

2.5 Chemical ordering

The extent of mixing (chemical order parameter), σ, may be defined as:[68]

$$\sigma = \frac{N_{AA} + N_{BB} - N_{AB}}{N_{AA} + N_{BB} + N_{AB}},$$ (14)

where N_{AA} and N_{BB} refer to the number of AA and BB nearest neighbour bonds within the binary cluster, and N_{AB} is the number of nearest-neighbour A–B bonds. The nearest neighbour cut-off is defined as the midpoint between the first and second neighbours, which for an FCC structure is: $(r_0 + \sqrt{2}r_0)/2$ (3.484 Å for Au). $\sigma = 1$ indicates complete separation, $\sigma \approx 0$ for disordered mixing, and $\sigma < 0$ indicates more ordered mixing, such as layering and onion-like configurations.[68]

3. Results and discussion

3.1 Chemical ordering for atomically doped systems

Pure monometallic nanoclusters were created, and the geometries minimised with respect to the energy. E_b^{Gupta} and E_b^{DFT} were calculated as 3.547 and 2.993 eV for Au, respectively; and 2.670 and 2.526 eV for Ag, respectively, highlighting significantly reduced bond strengths at the DFT level.

The most elementary combination of the two elements is to introduce a single dopant atom of a secondary species into the monometallic clusters, replacing one of the original atoms. We have investigated occupation of all the possible dopant sites for a single Au atom substituted into Ag_{147}, which results in a composition of Au_1Ag_{146}, and also repeated the opposite process for Ag included in Au_{147} to give $Au_{146}Ag_1$, with the results presented in Tables 2 and 3.

We performed calculations initially using the Gupta potentials. For Au_1Ag_{146}, the lowest energy configuration (E_{min}) is with the dopant Au atom occupying a subsurface vertex site, as shown in Fig. 2(a), with the next lowest energy arrangement ($E_{\text{min}-1}$) being the Au atom occupying a subsurface site below an edge [Fig. 2(b)]. Positioning of the Au dopant on (c) the (111) surface and (e) edge sites are greater in energy, implying reduced stability when the Au atom is on the surface ($E_{\text{tot}}^{\text{Gupta}} = 0.161$ and 0.228 eV, respectively). Given the lower surface energy and weaker binding of Ag compared to Au, these observations are understandable as the Au atom favours occupation of a highly coordinated site.

21052 | *Phys. Chem. Chem. Phys.*, 2014, **16**, 21049–21061

This journal is © the Owner Societies 2014

Table 2 Local atomic pressure (P_i) and energy (E_i) as a result of dopant atom position, i, for Au_1Ag_{146}, calculated using the Gupta potential. Structures (a)–(i) are given in order of decreasing relative total energy, ΔE_{tot}^{Gupta}, with the relative DFT energy given as ΔE_{tot}^{DFT}. $P_i > 0$ indicates compressive strain for the cluster, whilst $P_i < 0$ indicates tensile strain. For comparison, P_i and E_i are given for the same site, i, in Ag_{147}, denoted as $E_i^{Ag_{147}}$ and $P_i^{Ag_{147}}$, respectively. The change in pressure and energy are given as ΔP_i and ΔE_i, respectively. For the site descriptions the notation surf. and subsurf. are used for surface and subsurface sites, respectively

	ΔE_{tot}^{Gupta}/eV	Site description	$E_i^{Ag_{147}}$/eV	$P_i^{Ag_{147}}$/GPa	$E_i^{Au_1Ag_{146}}$/eV	$P_i^{Au_1Ag_{146}}$/GPa	ΔE_i/eV	ΔP_i/GPa	ΔE_{tot}^{DFT}/eV	Δq_i
(a)	0.000	Vertex, subsurf.	−2.255	−1.596	−3.268	−1.536	−1.013	0.060	0.089	0.203
(b)	0.124	Edge, subsurf.	−2.927	4.815	−3.316	−2.759	−0.388	−7.573	0.111	0.198
(c)	0.161	Centre of (111), surf.	−2.927	4.841	−3.112	−7.807	−0.184	−12.648	0.055	0.256
(d)	0.167	Centre of (100), subsurf.	−2.628	−4.759	3.333	−3.856	−0.705	0.902	0.069	0.210
(e)	0.228	Edge, surf.	−2.961	3.985	−2.932	−4.710	0.028	−8.695	0.042	0.311
(f)	0.250	Centre of cluster	−2.866	9.768	−3.338	2.121	−0.471	−7.647	0.083	0.259
(g)	0.262	Edge, two-layers subsurf.	−2.866	9.655	−3.349	0.141	−0.482	−9.515	0.038	0.269
(h)	0.269	Centre of (100), surf.	−2.960	4.062	−3.056	−7.177	−0.096	−11.239	0.036	0.294
(i)	0.309	Vertex, surf.	−2.208	−1.589	−2.710	−3.185	−0.502	−1.596	0.000	0.341

Table 3 Local atomic pressure (P_i) and energy (E_i) as a result of dopant atom position for $Au_{146}Ag_1$, calculated using the Gupta potential. Structures (j)–(r) are given in order of decreasing relative total energy, ΔE_{tot}^{Gupta}, with the relative DFT energy given as ΔE_{tot}^{DFT}. $P_i > 0$ indicates compressive strain for the cluster, whilst $P_i < 0$ indicates tensile strain. For comparison, P_i and E_i are given for the same site, i, in Au_{147}, denoted as $E_i^{Au_{147}}$ and $P_i^{Au_{147}}$, respectively. The change in pressure and energy are given as ΔP_i and ΔE_i, respectively. For the site descriptions the notation surf. and subsurf. are used for surface and subsurface sites, respectively

	ΔE_{tot}^{Gupta}/eV	Site description	$E_i^{Au_{147}}$/eV	$P_i^{Au_{147}}$/GPa	$E_i^{Au_{146}Ag_1}$/eV	$P_i^{Au_{146}Ag_1}$/GPa	ΔE_i/eV	ΔP_i/GPa	ΔE_{tot}^{DFT}/eV	Δq_i
(j)	0.000	Centre of (100), surf.	−3.778	5.521	−3.031	−5.297	0.747	−10.818	0.137	−0.243
(k)	0.020	Edge, two-layers subsurf.	−3.709	5.730	−3.373	16.749	0.336	11.019	0.113	−0.218
(l)	0.067	Edge, surf.	−3.778	5.427	−2.911	−3.546	0.867	−8.973	2.592	−0.077
(m)	0.067	Vertex, surf.	−3.181	−12.140	−2.670	−2.716	0.512	9.424	2.258	−0.075
(n)	0.078	Centre of cluster	−3.709	5.895	−3.349	21.960	0.360	16.065	0.148	−0.141
(o)	0.114	Centre of (111), surf.	−3.759	3.280	−3.105	0.305	0.654	−2.975	0.095	−0.278
(p)	0.118	Centre of (100), subsurf.	−3.501	−11.874	−3.358	15.527	0.143	27.401	0.031	−0.275
(q)	0.149	Edge, subsurf.	−3.759	3.244	−3.345	19.194	0.414	15.950	0.000	−0.284
(r)	0.298	Edge, subsurf.	−3.181	−12.147	−3.277	27.914	−0.096	40.060	0.017	−0.234

For each dopant site, i, the local atomic energy at the dopant positions (E_i) is given in Table 2 for the pure cluster and Au_1Ag_{146}, as well as the relative change in energy as a result of doping at each of these sites (ΔE_i). A decrease in energy is observed for most single dopant configurations (*i.e.* $\Delta E_i < 0$ eV), due to the increased strength of the Au–Ag interactions, with the exception being $\Delta E_i = 0.028$ eV for a surface edge.

In contrast, when substituting an Ag atom into Au_{147} to form $Au_{146}Ag_1$, the positioning of the Ag atom on the surface is energetically favoured. E_{min} is arranged with the Ag dopant occupying a site on the (100) face, whereas for E_{min-1} the Ag atom occupies a slightly off centre site within the cluster [Fig. 2(c) and (d)]. $\Delta E_i > 0$ eV, *i.e.* endothermic, for most $Au_{146}Ag_1$ arrangements, and thus it is not energetically favourable to introduce a single Ag atom, with ΔE_i values between 0.143 and 0.867 eV (Table 3). The only exception to this is for (r) in Table 3, where Ag is occupying a subsurface edge position.

To ascertain the possible causes of preferred dopant positioning, we calculated the local atomic pressure P_i for each dopant site using the Gupta potentials. P_i is defined as:

$$P_i = \frac{\partial E_i}{\partial V_i}, \tag{15}$$

where E_i is taken from as V_{clus} from eqn (2), and V_i is the bulk atomic volume, calculated using r_0. If $P_i < 0$, tensile strain exists, whereas $P_i > 0$ indicates compressive strain.
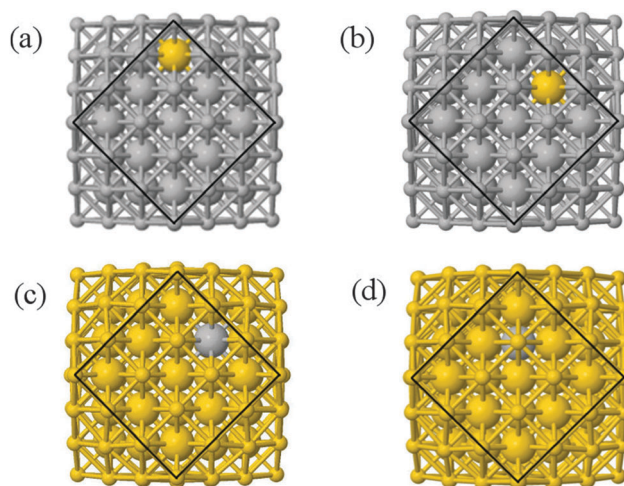

Fig. 2 Lowest energy arrangements for atomically doped structures: (a) $E_{min}^{Gupta}(Au_1Ag_{146})$; (b) $E_{min-1}^{Gupta}(Au_1Ag_{146})$; (c) $E_{min}^{Gupta}(Au_{146}Ag_1)$; (d) $E_{min-1}^{Gupta}(Au_{146}Ag_1)$. The outer geometric shell, or surface layer, is represented as ball-and-stick to emphasize the positioning of the dopant atom, with the atomic radius of the sub-surface atoms increased to highlight their depth. Both (a) and (b) have Au in a surface position, whilst (c) and (d) show Ag subsurface. Au and Ag atoms are represented by yellow and grey spheres, respectively.

The results of our calculations are listed in Tables 2 and 3 for Au_1Ag_{146} and $Au_{146}Ag_1$, respectively. For $E_{min}(Au_1Ag_{146})$, $\Delta P_i = 0.060$ GPa, however, for $E_{min-1}(Au_1Ag_{146})$, where the Au

occupies a sub-surface site below an edge, $\Delta P_i = -7.573$ GPa, and is accompanied by a corresponding decrease in bond lengths from the Au dopant to surface Ag (0.02–0.03 Å), and an increase in bond lengths from the Au dopant to other subsurface Ag (0.02–0.03 Å). ΔP_i also varies dramatically for $Au_{146}Ag_1$ depending on the site occupied by the dopant Ag: $\Delta P_i < 0$ for E_{min}, yet $\Delta P_i > 0$ for E_{min-1}. In general, ΔP_i decreases for doping of Ag_{147} with Au, and increases when doping Au_{147} with Ag, however there is a large variation in values, and thus it is difficult to correlate preferred positioning of the dopant atoms with the partial pressure encountered at each structural site.

Each atomically-doped system was reminimised using DFT, resulting in considerable reordering of the nanocluster energetics when compared to the semi-empirical potentials, as shown in Fig. 3. [DFT minima images are given in the ESI,† Fig. S1.] For Au_1Ag_{146}, the lowest energy DFT arrangement (E_{min}^{DFT}) is for the Au dopant to occupy a vertex position on the surface of the nanocluster, with the next lowest energy configuration (E_{min-1}^{DFT}) being the occupation of a (100) surface site, with an energy difference of 0.036 eV between the two arrangements (Table 2). This is in stark contrast to the Gupta potential, where positioning of the Au atom in a subsurface site is energetically beneficial.

Similarly, for $Au_{146}Ag_1$, the DFT calculations result in reordering of the most stable chemical arrangements (Table 3). E_{min}^{DFT} positions the Ag dopant in a subsurface edge site, and E_{min-1}^{DFT} places Ag also occupying a subsurface site, below a (100) surface, with an energy difference between the two of only 0.031 eV. These preferred chemical arrangements are again very different from the results of the Gupta potential, with the cohesive and surface energies seemingly less influential to the most stable chemical arrangements. The energetic reordering for the different chemical arrangements may therefore be attributed to alternative properties such as the partial charging of the dopant atom (Δq_i), which are not considered when using the semi-empirical potentials. To minimise electronic repulsion within monometallic nanoclusters, electrons tend to migrate to the surface, which may result in a negative partial charge on the vertex, edge and face atoms.[69] However, in bimetallic systems other factors can be influential, such as the electronegativities of the composite species, and charge transfer can influence the final shape and properties of the nanoalloy. Analysis of atomic charges were performed on each nanocluster using Bader analysis,[70] and the 147-atomic sites were analysed according to their structural position: face, edge, vertex or core, as given in Table 5. For both of the pure systems charge accumulates at the surface ($\Delta q > 0$ e), and charge depletion occurs in the core ($\Delta q < 0$ e), implying electron migration to the surface sites. The order of partial atomic charges for Ag_{147} are: $\Delta q_{vertex} > \Delta q_{edge} > \Delta q_{face}$, whereas for Au_{147} they are: $\Delta q_{vertex} > \Delta q_{face} > \Delta q_{edge}$. For both pure nanoclusters the least coordinated atomic sites (i.e. vertices) accumulate the greatest charge.

In comparison, for the atomically doped Au_1Ag_{146} system, Au atoms universally undergo charge accumulation, with the lowest energy structures also having the highest Δq_i for the dopant atom (0.341 and 0.294 for E_{min}^{DFT} and E_{min-1}^{DFT}, respectively). Improved stability of dopants is noted when the Au atom occupies a surface site at the DFT-level, and thus we conclude that there is a relationship between dopant coordination and the maximisation of Δq_i.

Complementary to the Au_1Ag_{146} analysis, in $Au_{146}Ag_1$ the Ag atoms undergo charge depletion (-0.284 and -0.275 for E_{min}^{DFT} and E_{min-1}^{DFT}, respectively), whilst the majority of Au surface atoms accumulate charge. The results from DFT calculations again correlate widely with Δq_i, except for arrangement (o) in Table 3. Additionally, we highlight improved stability of the Ag dopant when occupying subsurface sites, and therefore a balance between Δq_i and atomic coordination exists.

In general, the presence of a single dopant atom lowers E_{exc} of the cluster (ESI,† Table S1), with minor distortions to bond lengths ($<1\%$). Structurally, the Gupta potentials favour occupation of subsurface sites by Au atoms in Au_1Ag_{146}, whilst DFT methods prefer Au atoms occupying surface positions. No clear trend was observed for Ag atoms in $Au_{146}Ag_1$ using the Gupta potentials, but occupation of subsurface positions for Ag atoms are favoured by DFT methods. The dominating factor in determining the DFT relative total energy (E_{tot}^{DFT}) appears to be Δq_i. However, with the preferential positioning of Au being surface, and Ag being subsurface, we note that there is a correlation between both the atomic coordination and electron transfer. Though there is no clear connection between energetic ordering and the minimisation of ΔP_i, this is perhaps unsurprising given the similar atomic radii of Au and Ag. Furthermore, we were able to highlight that charge accumulation and depletion
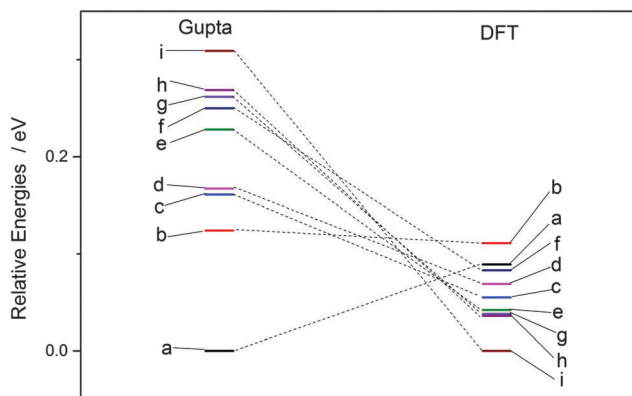

Fig. 3 Energetic reordering of Au_1Ag_{146}, where a–i represent differing dopant positions, as given in Table 2. In general, the energetic competition between isomers is closer at the DFT level than Gupta.

Table 4 Differences in E_b (ΔE_b) between alloy and core@shell structures for Gupta and DFT calculations. Positive values indicate the alloy is lower in energy than the core@shell arrangement

Structure	ΔE_b^{Gupta}/eV	ΔE_b^{DFT}/eV
$Au_{13}Ag_{134}$	0.027	0.001
$Au_{55}Ag_{92}$	0.015	0.016
$Au_{92}Ag_{55}$	0.003	−0.019
$Au_{134}Ag_{13}$	0.050	0.002

21054 | Phys. Chem. Chem. Phys., 2014, 16, 21049–21061

This journal is © the Owner Societies 2014

Table 5 Mean change in charge (Δq) for the core, face, edge and vertex positions for the lowest energy structures at the Gupta level, recalculated using DFT. Units are electrons, with negative values indicating charge depletion and positive values accumulation. Also given is the disorder parameter, σ, as described in eqn (14)

Structure	σ	Δq_{core}	Δq_{face}	Δq_{edge}	Δq_{vertex}
Ag_{147}	1.000	−0.030	0.014	0.007	0.072
Au_1Ag_{146}	0.964	−0.018	0.004	0.001	0.067
$Au_{13}Ag_{134}$	0.539	0.035	−0.012	−0.026	−0.025
$Au_{13}@Ag_{134}$	0.745	−0.015	−0.007	0.009	0.052
$Au_{55}Ag_{92}$	0.021	0.143	−0.087	−0.091	−0.064
$Au_{55}@Ag_{92}$	0.309	0.077	−0.070	−0.055	0.046
$Au_{74}Ag_{73}$	−0.036	0.117	−0.119	−0.090	0.143
$Au_{92}Ag_{55}$	0.064	0.088	0.154	−0.019	0.083
$Ag_{55}@Au_{92}$	0.309	−0.129	0.062	0.079	0.110
$Au_{134}Ag_{13}$	0.655	0.013	−0.080	0.030	0.034
$Ag_{13}@Au_{134}$	0.745	−0.043	0.014	0.018	0.085
$Au_{146}Ag_1$	0.964	−0.045	0.003	0.028	0.086
Au_{147}	1.000	−0.050	0.017	0.022	0.089

occurred for Au and Ag dopant atoms respectively, as is perhaps expected given their differing electronegativities.

3.2 Chemical ordering for Au_nAg_{147-n} nanoalloys

For a greater quantity of secondary species n, and thus a more complex ordering landscape, basin-hopping searches using the Gupta potential are performed to gain optimised chemical ordering. A preference for alloy arrangements is observed in the lowest energy structures, with a maximised number of Au–Ag interactions, and therefore larger E_b^{Gupta}. Experimentally, alloy arrangements can result in compromised rather than enhanced catalytic abilities, and thus the combination of two metals does not always produce a desirable synergistic effect.[71] For this reason, the controlled synthesis of core@shell structures is of great interest, and so we utilised the layered structure of the CO to create core@shell arrangements with complete shells of varying thickness, thus enabling comparison of the properties for core@shell chemical arrangements to the alloy arrangements.

In the structures identified as lowest energy from the basin-hopping searches, there are alloy arrangements with Au atoms preferentially occupying sub-vertex positions within the nano-alloys (Fig. 4). This shows some correlation with recent work by Bochicchio et al.[72] on size-mismatched systems, where the dopant atom relieves the pressure in the subvertex position. However, we have already highlighted in Section 3.1 that positioning of Au atoms in sub-vertex lattice sites leads only to the reduction of interatomic bond distances and the formation of more (stronger) Au–Ag interactions for AuAg nanoclusters. The subsurface positions are fully occupied by Au dopants for $n = 13$ or larger, which results in a sub-layer of Au atoms and a triple-layered chemical ordering (Ag@Au@Ag) in exceptional cases; this is particularly apparent for the 55 : 92 ratio of Au : Ag (ESI,† Fig. S2). As Au content is increased beyond 55 atoms, gold atoms then begin to also occupy the surface sites. σ is above 0 in all cases, which indicates that disordered mixing is preferred over ordered mixing.
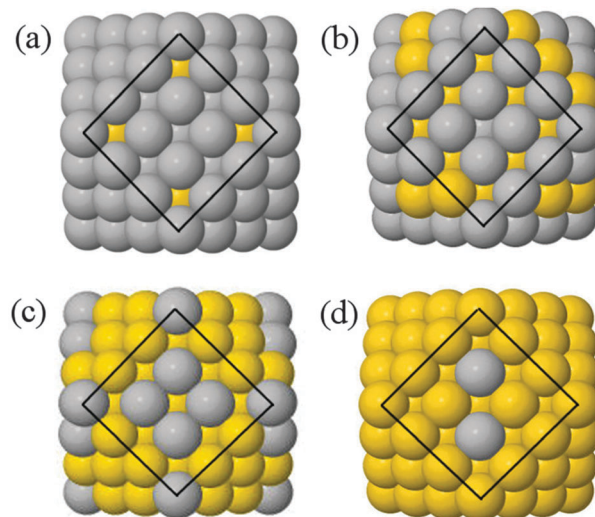

Fig. 4 Minimum energy alloy structures of cuboctahedral as calculated using atomic-swap basin-hopping with the Gupta potentials: (a) $Au_{13}Ag_{134}$, (b) $Au_{55}Ag_{92}$, (c) $Au_{92}Ag_{55}$ and (d) $Au_{134}Ag_{13}$. Yellow spheres represent Au, grey spheres Ag.

Overall, E_b^{Gupta} increases linearly with increasing Au content, from 2.669 eV (Ag_{147}) up to 3.541 eV (Au_{147}), in line with Vegard's law (Fig. 5).[73,74] This is unsurprising given the bond
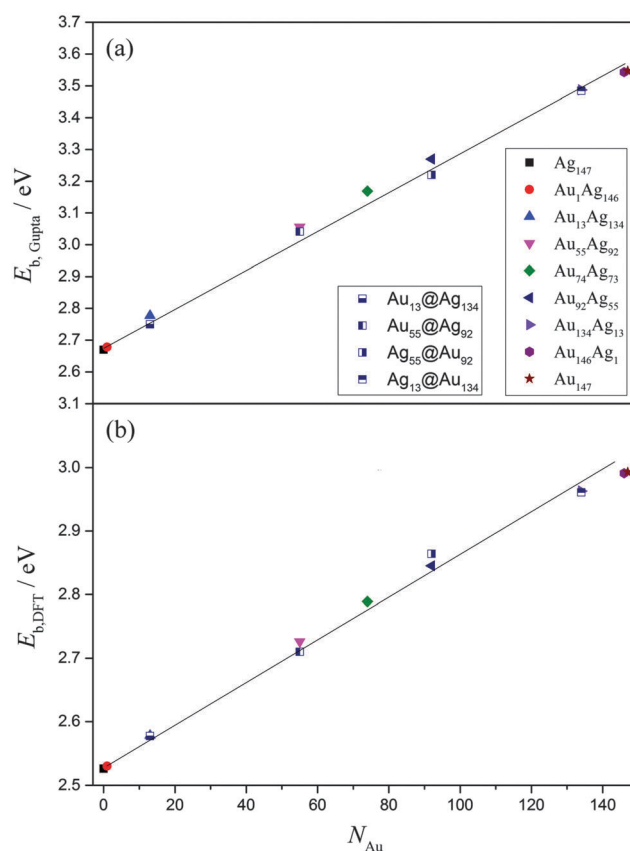

Fig. 5 (a) E_b^{Gupta} and (b) E_b^{DFT} as a function of Au content, N_{Au}. The lines are given as a guide to the eye. A key to the symbols is also provided in (a).

strengths at the Gupta level are: Au–Au (2.82 eV) > Au–Ag (1.81 eV) > Ag–Ag (1.36 eV), with values in parentheses given for the dimer pairs. The core@shell arrangements have similar energies to the alloy arrangements, as shown in Table 4, however at the Gupta-level all alloy arrangements are lower in energy. The same linear trend for E_b^{DFT} is apparent when the energies of the lowest-energy alloys are recalculated using DFT, as presented in Fig. 5 and Table S1 of the ESI.† Dimer bond strengths are Au–Au (2.68 eV) > Au–Ag (2.57 eV) > Ag–Ag (2.16 eV) in this case, and so the energetic ordering of bonds does not change. Importantly, we note that the core@shell arrangement for $Ag_{55}@Au_{92}$ has a lower DFT energy than the alloy equivalent, whereas all other core@shell arrangements are higher in energy than the alloy chemical orderings. In general, the energy difference between the core@shell and alloy structures is not large [$\leq$0.05 eV (Gupta) and $\leq$0.02 eV (DFT)], as highlighted in Table 4; and as mentioned previously, restructuring from core@shell geometries requires a great deal of energy (>2 eV), and thus if segregated structures are formed initially, the chemical ordering would be relatively stable under ambient conditions, and in the absence of surface reactions.

The propensity of $(AuAg)_{147}$ to prefer an alloy arrangement at the Gupta level is confirmed when comparing E_b^{Gupta} with σ (ESI,† Fig. S3). $Ag_{55}@Au_{92}$ has a greater value of σ than the alloy arrangement, $Au_{92}Ag_{55}$, as expected for a more segregated arrangement, yet has a lower E_b^{Gupta}; the observation is made for $Au_{55}Ag_{92}$ in comparison to $Au_{55}@Ag_{92}$. At the DFT-level, $Au_{55}Ag_{92}$ again has a lower E_b^{DFT} in comparison to the corresponding alloy, however $Ag_{55}@Ag_{92}$ has a higher E_b^{DFT} than its corresponding alloy, showing that DFT favours the Ag@Au arrangement for the 55 : 92 ratio. We note, however, that the energy differences are too small to make the same generalisations for the 13 : 134 ratio.

The energetic preference, at the DFT level, for Au surface segregation may be due to the improved charge transfer to Au atoms if they are the outermost species in the nanocluster, as discussed in Section 3.1; the electrons will naturally migrate to the surfaces to increase their degrees of freedom. Therefore, we have examined the extent of charge transfer occurring within each nanoalloy and core@shell structure presented.

Alloy arrangements exhibit disordered mixing ($\sigma \approx 0$), yet have the greatest changes in charge (Δq) when Ag is the dominant element in the composition: for instance, Δq_{face} is greater for both $Au_{13}Ag_{134}$ (0.012) and $Au_{55}Ag_{92}$ (0.087) in comparison to the core@shell equivalents, $Au_{13}@Ag_{134}$ (0.007) and $Au_{55}@Ag_{92}$ (0.070), as a greater number of surface Au–Ag interactions exist between the surface Ag and subsurface Au atoms (Table 5). Further analysis of the onion-like $Au_{55}Ag_{92}$ structure shows there is a combination of both charge depletion and charge accumulation at the surface, but in the sub-surface Au shell (42 atoms) charge accumulation occurs, and the inner Ag core (13 atoms) is charge depleted, as shown in Fig. 6. Whilst most of the core@shell structures favour charge accumulation at the surface, the degree of charge transfer is determined by whether Au or Ag occupies the surface layer of the nanocluster. Alloy arrangements exhibit a trade-off between
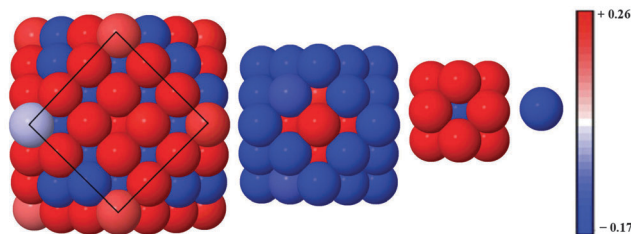

Fig. 6 Alloy structure of $Au_{55}Ag_{92}$ showing charge accumulation and depletion. As one moves left to right: 147 atoms; 55 atoms; 13 atoms and 1 atom for Ag@Au@Ag system. Red spheres represent charge depletion ($\Delta q_i > 0$), whilst blue spheres represent atoms with charge accumulation ($\Delta q_i < 0$). A charge colour scale is also given.

the additional electronic degrees of freedom at the surface and the contrasting electronegativities of Au and Ag: $Au_{13}Ag_{134}$ exhibits this compromise, with charge accumulation only occurring at the Ag vertices, with any remaining Ag atoms undergoing charge depletion; within the sub-surface Au there is charge accumulation. All the core@shell structures exhibit charge accumulation at the vertices. $Au_{55}@Ag_{92}$ undergoes charge depletion on faces and edges ($\Delta q_{face} = -0.070$, $\Delta q_{edge} = -0.055$), whilst the inverse structure, $Ag_{55}@Au_{92}$, has considerable charge accumulation at the surface ($\Delta q_{face} = 0.062$, $\Delta q_{edge} = 0.079$). $Au_{13}@Ag_{134}$ and $Ag_{13}@Au_{134}$ also exhibit similar behaviour to a lesser extent, with charge accumulation only on the vertices for the Ag shell, but Δq_{edge} and $\Delta q_{vertex} > 0$ for the Au shelled nanoclusters. This variation is perhaps due to the differing electronegativities of Ag (1.93) and Au (2.54), and thus charge transfer occurs from Ag to Au.

In summary, all nanoclusters experience charge accumulation at the lowest coordination sites in the nanocluster, irrespective of chemical ordering. Core@shell systems illustrate a greater change in atomic partial charges, as shown when comparing 55 : 92 systems to the 13 : 134 systems, due to the segregation of chemical species. In general, charge accumulates on Au, whereas charge depletes from Ag, in the alloys and core@shell arrangements, similar to our observations for single dopants.

3.3 Stability of Au_nAg_{147-n} nanoalloys

We have discussed the properties of core@shell and energetically favourable alloy chemical arrangements for Au_nAg_{147-n}. Attention is needed, however, to the relative stability of the different compositions, and chemical orderings, with respect to the pure nanoclusters, as agglomeration and chemical reactivity may occur in experimental environments, which would alter the structure and stoichiometry of the nanoclusters. Therefore, we plot Δ_{147}^{Gupta} and Δ_{147}^{DFT} as a function of N_{Au} in Fig. 7(a) and (b), respectively, with the most stable chemical arrangements positioned at the minima.

For the semi-empirical calculations, $Au_{55}Ag_{92}$ has the lowest Δ_{147}^{Gupta}, and may therefore be considered the most stable structure with respect to the formation of surfaces, which are approximated as $N^{2/3}$ in eqn (10) and (11). In general, Δ_{147}^{Gupta} follows a 'U-shaped' trend with increasing N_{Au}, but $Ag_{55}@Au_{92}$ is a clear
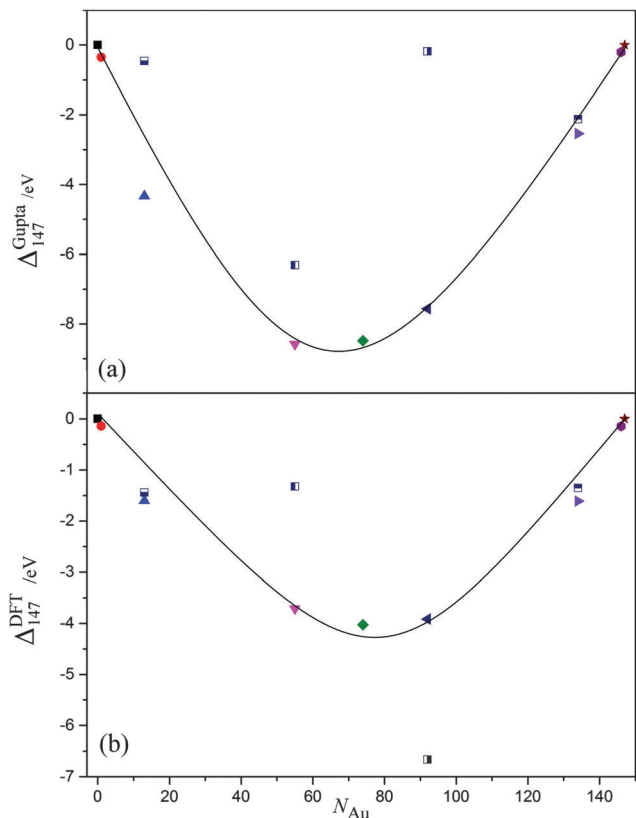
21056 | *Phys. Chem. Chem. Phys.*, 2014, **16**, 21049–21061

This journal is © the Owner Societies 2014

Fig. 7 (a) $\Delta_{147}^{\text{Gupta}}$ and (b) $\Delta_{147}^{\text{DFT}}$ as a function of Au content, N_{Au}. The black line is given as a guide to the eye; symbols are the same as given in Fig. 5.

anomaly to this trend. As mentioned previously in Section 3.2, an Ag core is not thermodynamically favourable, due to low Ag–Ag bond strength and high Au surface energies, thus resulting in lower stability for $Ag_{55}@Au_{92}$.

The stability of $Au_{55}Ag_{92}$ may be attributed to the Ag@Au@Ag arrangement that the alloy takes: Au–Ag interactions are max-imised, and there is a corresponding reduction in the (weaker) Ag–Ag bonds. Nonetheless, the stability is not entirely depen-dent on the number of Au–Ag bonds, as $Au_{74}Ag_{73}$ is less stable despite having more Au–Ag interactions [$\sigma(Au_{92}Ag_{55}) = 0.064$, $\sigma(Au_{74}Ag_{73}) = -0.036$]. The difference is that $Au_{55}Ag_{92}$ has more surface Ag atoms, and thus there is an overall balance at the Gupta level between reducing surface energies and increasing binding energies. Of the core@shell systems, $Au_{55}@Ag_{92}$ has the lowest $\Delta_{147}^{\text{Gupta}}$ as it maximises the number of Au–Ag inter-actions, and has a thermodynamically favourable Au core. $Au_{13}@Ag_{134}$ has fewer Au–Ag interactions, thus lowering the stability of this arrangement.

In contrast, $Ag_{55}@Au_{92}$ has the lowest $\Delta_{147}^{\text{DFT}}$ as calculated at the DFT-level, by an energy of ~ 2.5 eV, which is surprising given that thermodynamic considerations would favour an Ag shell. The next most stable structure, $Au_{92}Ag_{55}$, has the same stoichio-metry but more Au–Ag bonds, adopting an Ag@Au@Au/Ag configuration, where the outermost shell is an alloyed layer of both Au and Ag atoms [$\sigma(Ag_{55}@Au_{92}) = 0.309$, $\sigma(Au_{92}Ag_{55}) = 0.064$]. The energetic preference of $Ag_{55}@Au_{92}$ for DFT may be

attributed to the Au surface being able to draw electron density from the Ag atoms more readily than if Au atoms were posi-tioned internally; we have seen from the single dopant calcula-tions for DFT methods in Section 3.1 that an Au atom prefers to be at the surface. Thus, as electrons migrate to the surface of the cluster due to the increased degrees of electronic freedom available, it also follows that Au would benefit from greater charge transfer when positioned at the surface. We find, there-fore, that overall stability is not only a case of maximisation of Au–Ag bonds and minimising surface energies of the nanocluster through specific chemical ordering, but a compromise of the ease at which Au can gain electrons. For DFT, the latter observable is prevalent in determining $\Delta_{147}^{\text{DFT}}$.

In summary, the stability of a nanoalloy at the Gupta-level is determined through a balance of maximising Au–Ag inter-actions and minimising the surface energy – it is more favour-able to have a greater proportion of the surface atoms as Ag rather than Au. However, when reminimised using DFT, the stability of the nanocluster is also dependent on maximal charge transfer from Ag to Au, and thus an Au shell is more favourable than initially thought due to the increased degrees of electronic freedom at the surface.

3.4 Electronic properties

In the context of using these AuAg nanoclusters as semiconductor-supported co-catalysts in photocatalytic reac-tions, such as the reduction of hydrogen, it is known that the introduction of a co-catalyst results in a shift of the E_F towards the conduction band (CB) of the semiconductor, indicating improved reductive ability.[75] The possibility of screening sui-table nanoclusters through a band alignment procedure, where the density of states (DOS) of the nanocluster are aligned against the band structure of the support, as illustrated in Fig. 8 using the work functions of different bulk Au and Ag surfaces (given in Table 6), is therefore possible.[76] Au may exhibit better catalytic activity than Ag in this context, due to the greater work function of ~ 5.4 eV compared to ~ 4.6 eV, respectively; this places E_F of Au below the conduction band
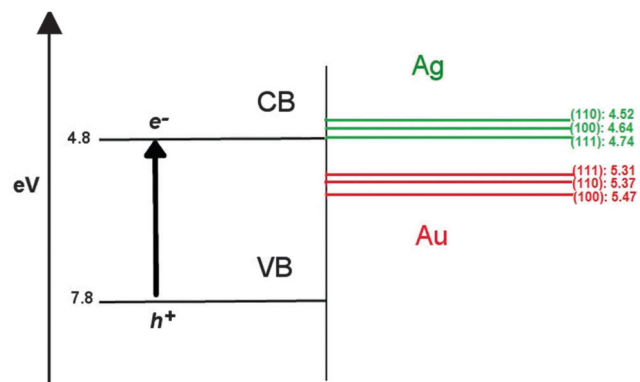

Fig. 8 The differing work functions of Au and Ag surfaces in comparison to bulk TiO_2 (rutile), showing that Au is more likely to accept an electron than Ag. Differing surfaces are noted in parentheses, all other values are given in eV.

Table 6 Work functions (Φ) for differing Au and Ag surfaces (eV)

Surface	Φ Ag	Φ Au
(100)	4.64	5.47
(110)	4.52	5.37
(111)	4.74	5.31

minimum (CBM) of popular semiconducting supports such as TiO$_2$, which would allow an electron to "drop" in energy should it transfer from the oxide conduction band to the unoccupied states of the nanocluster. Ag, however, would require an overpotential for the same electron transfer to occur, as E_F of Ag is above the TiO$_2$ CBM, making Ag less likely to accumulate photo-excited electrons and contribute to H reduction.

For an electron to be transferred to the co-catalyst from a semiconductor, the unoccupied surface d-orbitals of the nanocluster must be readily accepting of, and lower in energy than the photo-excited electrons in the CB of the support. If there were no unoccupied d-orbitals available on the nanocluster surface, tunnelling of electrons would allow occupation of states on core atoms, though the probability of this decays exponentially with depth from the surface. So, for trapping of photo-excited electrons to occur, it is more favourable for surface atoms to have a positive partial charge, otherwise the process is dependent on electron tunnelling.

By this proposition, our observations in Section 3.2 imply that Au@Ag would most favour the acceptance of photo-excited electrons, due to the positive partial charges on the vertex and edge sites of the nanocluster surface. However, from the concept of work function alignment introduced in Fig. 8, one would expect Ag@Au to be more suitable, as an Au shell would lead to a lower E_F, and thus more energetically accessible states for an additional incoming electron. In order to address these topics, we have examined the DOS profiles of all systems, specifically the d-orbitals, which we have decomposed into projected contributions from core and shell atoms, and considered the position of the unoccupied d-orbitals with respect to E_F.

E_F for Au$_{147}$ and Ag$_{147}$ is calculated as -4.830 eV and -3.996 eV, respectively, matching the difference between bulk Au and Ag in Table 6. Fig. 9(a) shows Ag$_{147}$ has less unoccupied d-orbitals on the surface atoms than Au [Fig. 9(b)], and when analysed alongside the high E_F one would hypothesise that Ag$_{147}$ would be unsuitable for use in co-catalysed photocatalytic reactions. Au$_{147}$ has more unoccupied d-states than Ag$_{147}$ at E_F, but the difference is so small that one would not expect this alone to account for the reported catalytic activity observed in experiments.[4] However, the proximity of E_F for Au$_{147}$ to the CBM of both rutile and anatase could account for any enhanced activity, especially when one considers surface effects on the electronic structure of the support, such as upward band-bending. Introduction of a single Ag atom, to form Au$_{146}$Ag$_1$, results in negligible increases in the d-orbital contributions at E_F, by 0.16 states, whereas the introduction of a single Au atom to Ag$_{147}$ results in the reverse effect for Au$_1$Ag$_{146}$. Furthermore, the DOS profile for Au$_{74}$Ag$_{73}$ appears to be an average of the
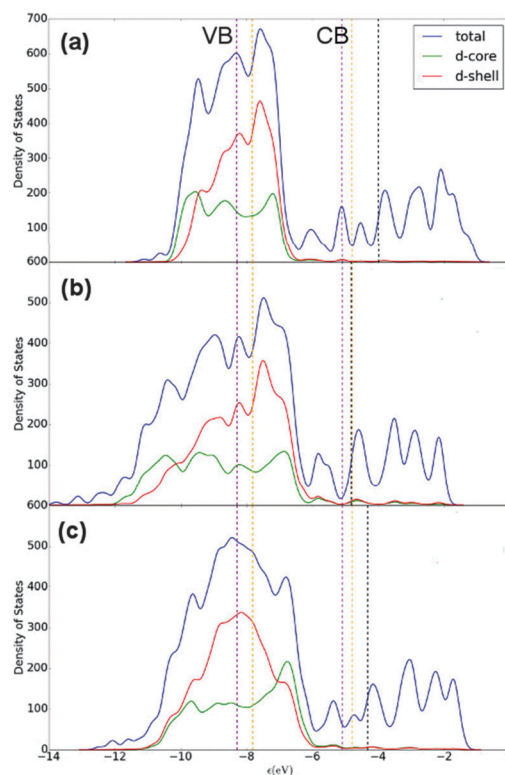
Fig. 9 Density of states (DOS) profiles for (a) Ag$_{147}$, (b) Au$_{147}$ and (c) Au$_{74}$Ag$_{73}$. A key is provided. E_F is given as a black dotted line, with the valence band maximum (VBM) and conduction band minimum (CBM) in purple and orange for anatase and rutile TiO$_2$, respectively.[77] A Gaussian broadening of 0.05 eV has been used on the electronic states.

composite species, with E_F also positioned at an intermediate value of -4.335 eV.

Alloy structures marginally increase the quantity of unoccupied d-states at E_F, in comparison to their corresponding core@shell arrangements (with the exception of Au$_{13}$Ag$_{134}$/ Au$_{13}$@Ag$_{134}$), as illustrated in the ESI† (Fig. S4 and S5). For instance, Au$_{55}$Ag$_{92}$ has 10.06 unoccupied d-states (d-core and d-shell) at E_F, in comparison to 8.89 for Au$_{55}$@Ag$_{92}$. There is a greater quantity of unoccupied d-states at E_F for Au$_{92}$Ag$_{55}$ than for Ag$_{55}$@Au$_{92}$ (13.91 vs. 11.5 d-orbitals at E_F). Decomposing the number of unoccupied d-orbitals into core and shell contributions shows that Ag$_{55}$@Au$_{92}$ has a greater number of unoccupied d-orbitals in the shell than Au$_{55}$@Ag$_{92}$ (11.13 vs. 2.71 at E_F). The same trend is observed for the 13 : 134 ratios, where Ag$_{13}$@Au$_{134}$ has 8.61 d-orbital states just above E_F, and Au$_{13}$@Ag$_{134}$ has only 3.13, respectively.

Despite the differences in available d-orbitals between core@shell and alloy arrangements being marginal, a noticeable shift in E_F is also observed: for core@shell structures E_F is closest to that of the shell species in all cases – for instance, E_F for Au$_{55}$@Ag$_{92}$ is -4.039 eV whilst for Ag$_{147}$ E_F is -3.966 eV (ESI,† Table S1).

In summary, the differences in E_F for monometallic species replicate bulk differences, and for single dopant systems minimal changes occur to the electronic structure of the system;

21058 | *Phys. Chem. Chem. Phys.*, 2014, **16**, 21049–21061

This journal is © the Owner Societies 2014

Furthermore, Au$_{74}$Ag$_{73}$ displays properties that are an average of the two pure systems. Core@shell structures offer more desirable features than the alloy nanoclusters for co-catalysed photocatalysis, with a greater number of available unoccupied d-orbitals close to E_F and marginally greater numbers of unoccupied d-orbitals were observed for Ag@Au compositions than for Au@Ag; however, the change in d-orbitals for bimetallic nanoclusters is still very low for all compositions investigated and thus further work is necessary to understand the successful photocatalytic applications of these nanoclusters.

4. Conclusions

We have presented a thorough examination of the optimised chemical orderings for cuboctahedral (AuAg)$_{147}$ nanoalloys, with the aim being to highlight thermodynamically stable structures and to discuss their desirable properties for photo-catalytic applications. In general, alloy structures are more thermodynamically stable at the Gupta level, as these maximise Au–Ag interactions. Au was found to favourably occupy sub-vertex positions within the alloy nanoclusters, as this maximises stronger Au–Ag interactions. This effect leads to onion-like structures forming, e.g. Ag@Au@Ag, as seen previously for AuPd.[78] However, at the DFT-level, Au atoms are instead found to favour surface sites, with Ag$_{55}$@Au$_{92}$ being the most energetically favourable investigated. This may be attributed to the fact that the Au atoms can draw electron density more easily when positioned in the geometric shell, as electrons will naturally migrate towards the surface. The difference in binding energies between alloy and core@shell structures at equivalent stoichiometries is small, and thus both structures can be assumed to be energetically stable. Charge transfer between core@shell arrangements is of an interfacial nature, and thus influences from the core are more pronounced for thin shells, allowing for co-catalyst design. From thermodynamic arguments, Au is favoured at the core, and Ag at the surface in core@shell structures, due to the differing surface and cohesive energies. However, at the DFT-level, Bader analysis shows that Au@Ag results in electron depletion at the surface, and overall instability compared to Ag@Au, and further analysis is needed to understand if this effect would result in alternative alloy arrangements at the DFT level of theory.

Electronic properties were examined for the applicability of different chemical orderings to co-catalysed photocatalysis, however none of the structures investigated display desirable properties as encountered for systems such as AuPd.[79,80] At best, a shift in E_F is observed for (AuAg)$_{147}$ as a result of combining the two metals, indicative of a capability to extend the lifetime of photo-excited electrons beyond that which is found for isolated Ag$_{147}$ nanoclusters. E_F of bimetallic systems is closest to that of the shell species in all cases. Despite the lack of unoccupied d-orbitals in the structures investigated, the experimental photocatalytic activity could be fine-tuned through pre-treatment experimental processes such as surface oxidation and is subject to on-going investigation.

Acknowledgements

Notes and references

1 A. Abad, A. Corma and H. García, *Chem. – Eur. J.*, 2008, **14**, 212–222.
2 D. I. Enache, D. W. Knight and G. J. Hutchings, *Catal. Lett.*, 2005, **103**, 43–52.
3 G. A. Somorjai and J. Y. Park, *Top. Catal.*, 2008, **49**, 126–135.
4 A. Primo, A. Corma and H. García, *Phys. Chem. Chem. Phys.*, 2011, **13**, 886–910.
5 C. Gomes Silva, R. Juárez, T. Marino, R. Molinari and H. García, *J. Am. Chem. Soc.*, 2010, **133**, 595–602.
6 M. Jakob, H. Levanon and P. V. Kamat, *Nano Lett.*, 2003, **3**, 353–358.
7 R. Ferrando, J. Jellinek and R. L. Johnston, *Chem. Rev.*, 2008, **108**, 845–910.
8 D. Mott, N. T. B. Thuy, Y. Aoki and S. Maenosono, *Philos. Trans. R. Soc., A*, 2010, **368**, 4275–4292.
9 S. Nishimura, A. T. N. Dao, D. Mott, K. Ebitani and S. Maenosono, *J. Phys. Chem. C*, 2012, **116**, 4511–4516.
10 J. Jellinek and E. B. Krissinel, *Chem. Phys. Lett.*, 1996, **258**, 283–292.
11 J. Jellinek, *Theory of atomic and molecular clusters: with a glimpse at experiments*, Springer, 1999.
12 F. Pittaway, L. O. Paz-borbo, R. L. Johnston, H. Arslan, R. Ferrando, C. Mottet, G. Barcaro and A. Fortunelli, *J. Phys. Chem.*, 2009, **113**, 9141–9152.
13 M. T. Oakley, R. L. Johnston and D. J. Wales, *Phys. Chem. Chem. Phys.*, 2013, **15**, 3965–3976.
14 A. Rapallo, G. Rossi, R. Ferrando, A. Fortunelli, B. C. Curley, L. D. Lloyd, G. M. Tarbuck and R. L. Johnston, *J. Chem. Phys.*, 2005, **122**, 194308.
15 V. Moreno, J. Creuze, F. Berthier, C. Mottet, G. Tréglia and B. Legrand, *Surf. Sci.*, 2006, **600**, 5011–5020.
16 F. Baletto, R. Ferrando, A. Fortunelli, F. Montalenti and C. Mottet, *J. Chem. Phys.*, 2002, **116**, 3856.
17 G. Rossi, R. Ferrando, A. Rapallo, A. Fortunelli, B. C. Curley, L. D. Lloyd and R. L. Johnston, *J. Chem. Phys.*, 2005, **122**, 194309.
18 T. P. Martin, *Phys. Rep.*, 1996, **273**, 199–241.

This journal is © the Owner Societies 2014

Phys. Chem. Chem. Phys., 2014, **16**, 21049–21061 | 21059

19 G. A. Somorjai, B. Chaudret, P. Serp and K. Philippot, *Nanomaterials in Catalysis*, John Wiley & Sons, 2012.

20 J. Doye and D. Wales, *J. Chem. Soc., Faraday Trans.*, 1997, **93**, 4233–4243.

21 M. M. Mariscal, O. A. Oviedo and E. P. M. Leiva, *Metal Clusters and Nanoalloys: From Modeling to Applications*, Springer, New York, 2012.

22 W. de Heer, *Rev. Mod. Phys.*, 1993, **65**, 611–676.

23 T. Déronzier, F. Morfin, M. Lomello and J.-L. Rousset, *J. Catal.*, 2014, **311**, 221–229.

24 C. Wang, H. Yin, R. Chan, S. Peng, S. Dai and S. Sun, *Chem. Mater.*, 2009, **21**, 433–435.

25 W. M. Haynes, D. R. Lide and T. J. Bruno, *CRC Handbook of Chemistry and Physics 2012-2013*, CRC press, 2012.

26 L. Lu, H. Wang, Y. Zhou, S. Xi, H. Zhang, J. Hu and B. Zhao, *Chem. Commun.*, 2002, 144–145.

27 R. T. Tom, A. S. Nair, N. Singh, M. Aslam, C. L. Nagendra, R. Philip, K. Vijayamohanan and T. Pradeep, *Langmuir*, 2003, **19**, 3439–3445.

28 S. Anandan, F. Grieser and M. Ashokkumar, *J. Phys. Chem. C*, 2008, **112**, 15102–15105.

29 H.-L. Jiang, T. Akita, T. Ishida, M. Haruta and Q. Xu, *J. Am. Chem. Soc.*, 2011, **133**, 1304–1306.

30 F. Cleri and V. Rosato, *Phys. Rev. B: Condens. Matter Mater. Phys.*, 1993, **48**, 22.

31 B. C. Curley, G. Rossi, R. Ferrando and R. L. Johnston, *Eur. Phys. J. D*, 2007, **43**, 53–56.

32 C. Kittel and P. McEuen, *Introduction to solid state physics*, Wiley, New York, 1996, vol. 7.

33 F. Chen and R. L. Johnston, *Acta Mater.*, 2008, **56**, 2374–2380.

34 I. L. Garzón, K. Michaelian, M. R. Beltrán, A. Posada-Amarillas, P. Ordejón, E. Artacho, D. Sánchez-Portal and J. M. Soler, *Phys. Rev. Lett.*, 1998, **81**, 1600.

35 G. Bravo-Pérez, I. L. Garzón and O. Novaro, *THEOCHEM*, 1999, **493**, 225–231.

36 N. T. Wilson and R. L. Johnston, *Eur. Phys. J. D*, 2000, **12**, 161–169.

37 J. Wang, G. Wang and J. Zhao, *Phys. Rev. B: Condens. Matter Mater. Phys.*, 2002, **66**, 35418.

38 J. Li, X. Li, H.-J. Zhai and L.-S. Wang, *Science*, 2003, **299**, 864–867.

39 V. Bonačić-Koutecký, M. Boiron, J. Pittner, P. Fantucci and J. Koutecký, *Eur. Phys. J. D*, 1999, **9**, 183–187.

40 M. N. Huda and A. K. Ray, *Eur. Phys. J. D*, 2003, **22**, 217–227.

41 M. N. Huda and A. K. Ray, *Phys. Rev. A*, 2003, **67**, 13201.

42 X. Yang, W. Cai and X. Shao, *J. Phys. Chem. A*, 2007, **111**, 5048–5056.

43 A. Desireddy, B. E. Conn, J. Guo, B. Yoon, R. N. Barnett, B. M. Monahan, K. Kirschbaum, W. P. Griffith, R. L. Whetten and U. Landman, *Nature*, 2013, **501**, 399–402.

44 G. F. Zhao and Z. Zeng, *J. Chem. Phys.*, 2006, **125**, 014303.

45 S. Heiles, A. J. Logsdail, R. Schäfer and R. L. Johnston, *Nanoscale*, 2012, **4**, 1109–1115.

46 V. Bonačić-Koutecký, J. Burda, R. Mitrić, M. Ge, G. Zampella and P. Fantucci, *J. Chem. Phys.*, 2002, **117**, 3120.

47 F. Baletto and R. Ferrando, *Rev. Mod. Phys.*, 2005, **77**, 371.

48 L. O. Paz-Borbón, R. L. Johnston, G. Barcaro and A. Fortunelli, *J. Chem. Phys.*, 2008, **128**, 134517.

49 M. Zhang and R. Fournier, *THEOCHEM*, 2006, **762**, 49–56.

50 F. Chen, B. C. Curley, G. Rossi and R. L. Johnston, *J. Phys. Chem. C*, 2007, **111**, 9157–9165.

51 M. Cerbelaud, R. Ferrando, G. Barcaro and A. Fortunelli, *Phys. Chem. Chem. Phys.*, 2011, **13**, 10232–10240.

52 F. Calvo, A. Fortunelli, F. Negreiros and D. J. Wales, *J. Chem. Phys.*, 2013, **139**, 111102.

53 R. P. Gupta, *Phys. Rev. B: Condens. Matter Mater. Phys.*, 1981, **23**, 6265.

54 F. Chen and R. L. Johnston, *Appl. Phys. Lett.*, 2008, **92**, 023112.

55 A. J. Logsdail and R. L. Johnston, *RSC Adv.*, 2012, **2**, 5863–5869.

56 A. J. Logsdail, Z. Y. Li and R. L. Johnston, *Phys. Chem. Chem. Phys.*, 2013, **15**, 8392–8400.

57 O. K. Andersen and O. Jepsen, *Phys. Rev. Lett.*, 1984, **53**, 2571–2574.

58 D. Wales and J. Doye, *J. Phys. Chem. A*, 1997, **101**, 5111–5116.

59 P. E. Blöchl, *Phys. Rev. B: Condens. Matter Mater. Phys.*, 1994, **50**, 17953.

60 J. J. Mortensen, L. B. Hansen and K. W. Jacobsen, *Phys. Rev. B: Condens. Matter Mater. Phys.*, 2005, **71**, 35109.

61 J. Enkovaara, C. Rostgaard, J. J. Mortensen, J. Chen, M. Dułak, L. Ferrighi, J. Gavnholt, C. Glinsvad, V. Haikola and H. A. Hansen, *J. Phys.: Condens. Matter*, 2010, **22**, 253202.

62 J. P. Perdew, K. Burke and M. Ernzerhof, *Phys. Rev. Lett.*, 1996, **77**, 3865.

63 R. Ismail and R. L. Johnston, *Phys. Chem. Chem. Phys.*, 2010, **12**, 8607–8619.

64 C. L. Cleveland and U. Landman, *J. Chem. Phys.*, 1991, **94**, 7376.

65 J. Uppenbrink and D. J. Wales, *J. Chem. Phys.*, 1992, **96**, 8520.

66 L. O. Paz-Borbón, R. L. Johnston, G. Barcaro and A. Fortunelli, *J. Phys. Chem. C*, 2007, **111**, 2936–2941.

67 G. Rossi and R. Ferrando, *J. Phys.: Condens. Matter*, 2009, **21**, 084208.

68 F. Aguilera-Granja, A. Vega, J. Rogan, X. Andrade and G. García, *Phys. Rev. B: Condens. Matter Mater. Phys.*, 2006, **74**, 224405.

69 X. Ma, Y. Dai, M. Guo, Y. Zhu and B. Huang, *Phys. Chem. Chem. Phys.*, 2013, **15**, 8722–8731.

70 G. Henkelman, A. Arnaldsson and H. Jónsson, *Comput. Mater. Sci.*, 2006, **36**, 354–360.

71 J. Sinzig, U. Radtke, M. Quinten and U. Kreibig, *Z. Phys. D: At., Mol. Clusters*, 1993, **26**, 242–245.

72 D. Bochicchio, F. Negro and R. Ferrando, *Comput. Theor. Chem.*, 2013, **1021**, 177–182.

73 L. Vegard, *Z. Phys. A: At. Nucl.*, 1921, **5**, 17–26.

74 L. Vegard, *Z. Kristallogr.*, 1928, **67**, 239–259.

75 N. Lopez and J. K. Nørskov, *J. Am. Chem. Soc.*, 2002, **124**, 11262–11263.

21060 | *Phys. Chem. Chem. Phys.*, 2014, **16**, 21049–21061

This journal is © the Owner Societies 2014

76 V. Pfeifer, P. Erhart, S. Li, K. Rachut, J. Morasch, J. Bro, P. Reckers, T. Mayer, S. Ru, A. Zaban, M. Sero, J. Bisquert, W. Jaegermann and A. Klein, *J. Phys. Chem. Lett.*, 2013, **4**, 4182–4187.

77 D. O. Scanlon, C. W. Dunnill, J. Buckeridge, S. A. Shevlin, A. J. Logsdail, S. M. Woodley, C. R. A. Catlow, M. J. Powell, R. G. Palgrave and I. P. Parkin, *Nat. Mater.*, 2013, **12**, 798–801.

78 D. Ferrer, D. A. Blom, L. F. Allard, S. Mejía, E. Pérez-Tijerina and M. José-Yacamán, *J. Mater. Chem.*, 2008, **18**, 2442–2446.

79 N. Dimitratos, J. A. Lopez-Sanchez, D. Morgan, A. F. Carley, R. Tiruvalam, C. J. Kiely, D. Bethell and G. J. Hutchings, *Phys. Chem. Chem. Phys.*, 2009, **11**, 5142–5153.

80 J. Pritchard, L. Kesavan, M. Piccinini, Q. He, R. Tiruvalam, N. Dimitratos, J. A. Lopez-Sanchez, A. F. Carley, J. K. Edwards, C. J. Kiely and G. J. Hutchings, *Langmuir*, 2010, **26**, 16568–16577.

This journal is © the Owner Societies 2014

Phys. Chem. Chem. Phys., 2014, **16**, 21049–21061 | **21061**